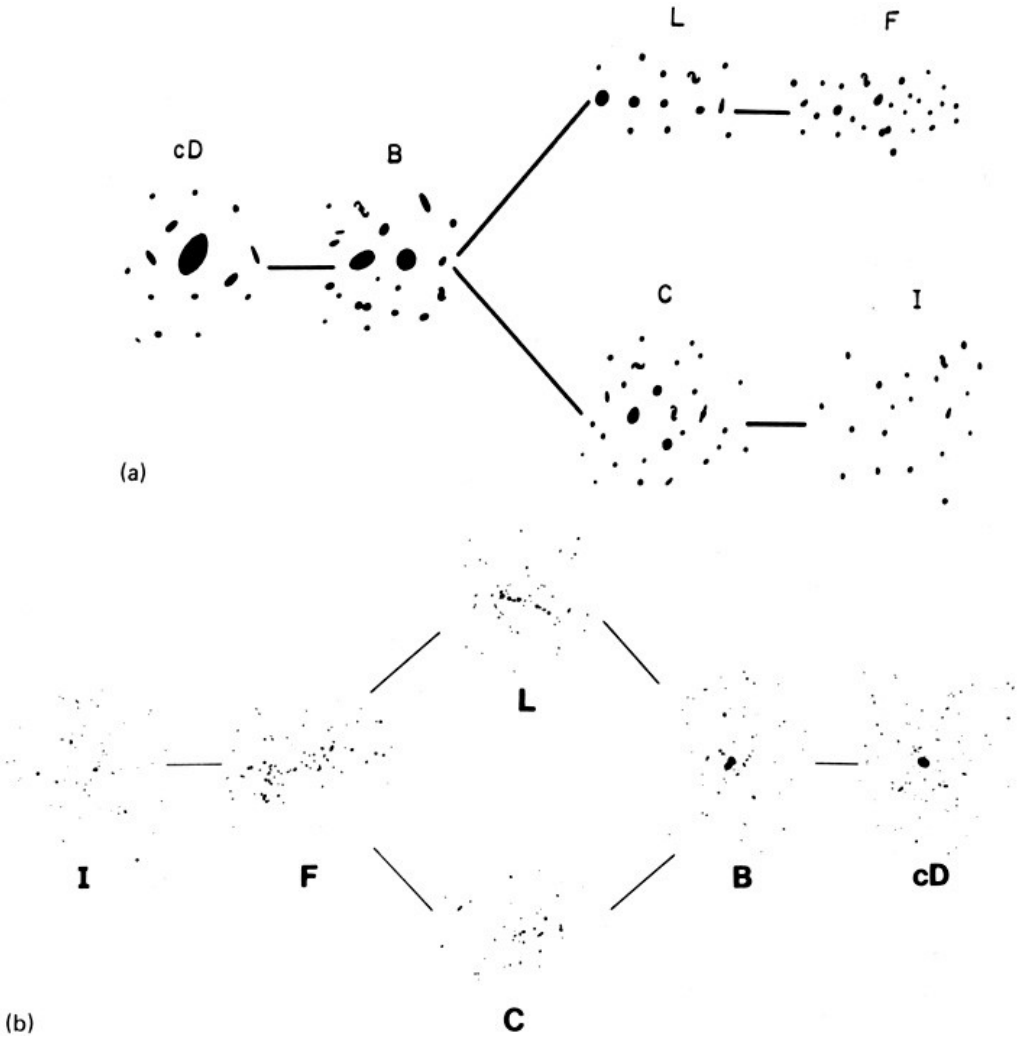
L
F
cD
B
C
I
(a)
L
I
F
B
cD
C
(b)

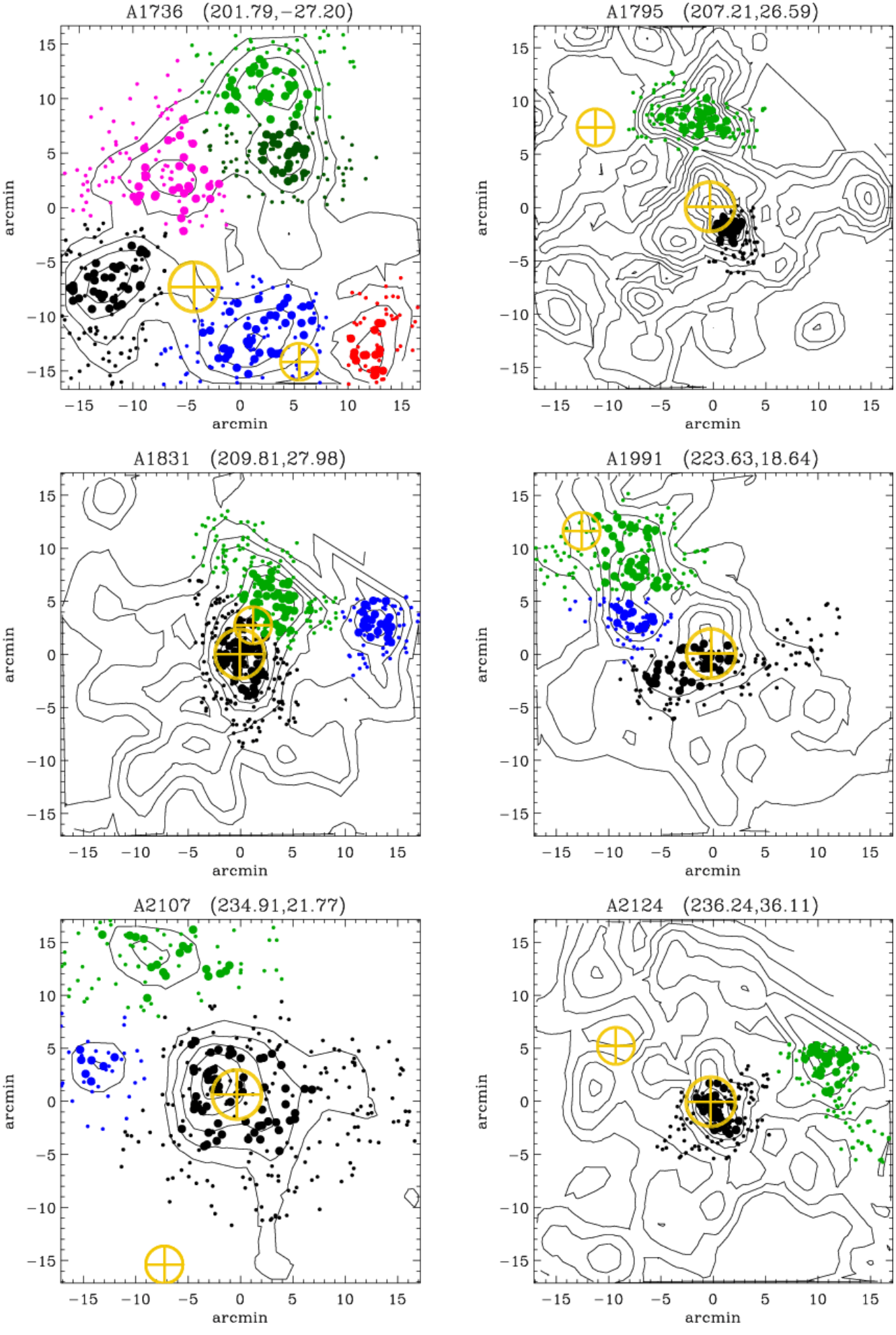
A1736 (201.79,−27.20)
A1795 (207.21,26.59)
A1831 (209.81,27.98)
A1991 (223.63,18.64)
A2107 (234.91,21.77)
A2124 (236.24,36.11)
arcmin
arcmin
15
10
5
0
−5
−10
−15

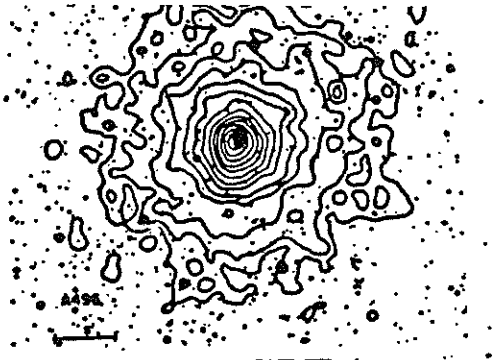

SINGLE

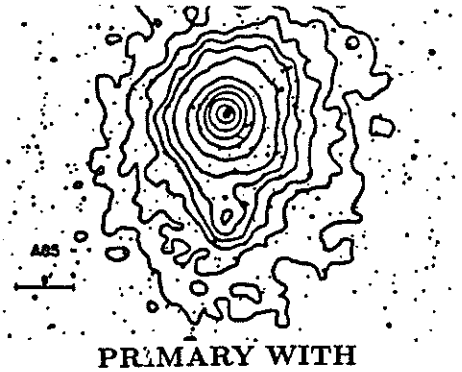

PRIMARY WITH SMALL SECONDARY

ELLIPTICAL

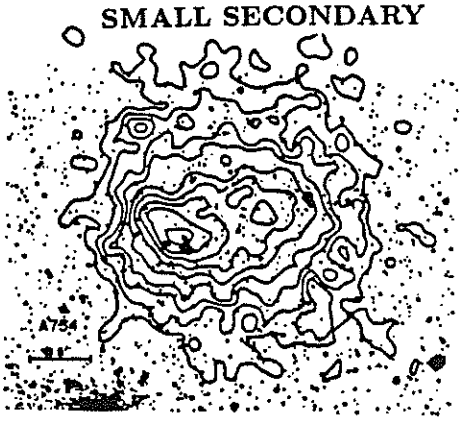

OFFSET CENTER

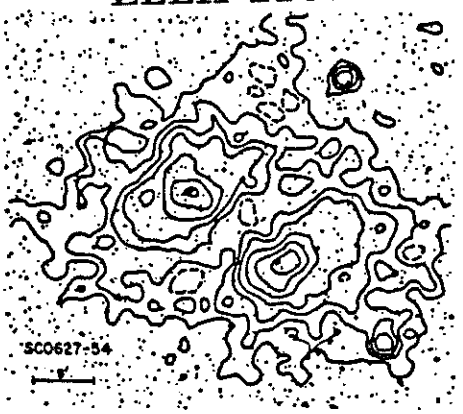

DOUBLE

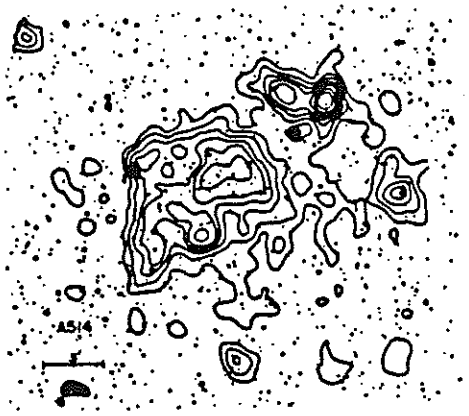

COMPLEX

Figure 11 shows x-ray isointensity contours superposed on optical sky prints for six x-ray defined cluster morphological classes.

Jones e Forman 82

(vedi anche Sarazin 86)

2.2. MERGER FREQUENCY OF ROSAT CLUSTERS

The result of computing power ratios for the brightest ~ 40 *ROSAT* clusters is displayed in Figure 3.8. It is immediately apparent that there is a marked deficiency of highly disturbed clusters (complex and double). These brightest clusters therefore lack young members and are instead dominated by mostly evolved clusters with only small-scale (< 500 kpc) substructure. Since such highly evolved clusters are usually associated with cooling flows it should be expected that cooling flows dominate the brightest clusters as has been suggested before on different grounds (e.g., Arnaud 1988; Forman & Jones 1990; Edge et al. 1992; Peres et al. 1998).

In Figure 3.9 the quantitative connection between cooling flows and cluster morphology is shown by the anti-correlation of the mass deposition rate ($\dot{M}$) and P_2/P_0. This represents the first quantitative description of the anti-correlation of substructure with the strength of a cooling flow. Note the large scatter for systems that have significant substructure (i.e., large P_2/P_0). Analysis of this correlation and its large scatter should shed light on how cooling flows are disrupted by mergers and are subsequently re-established.

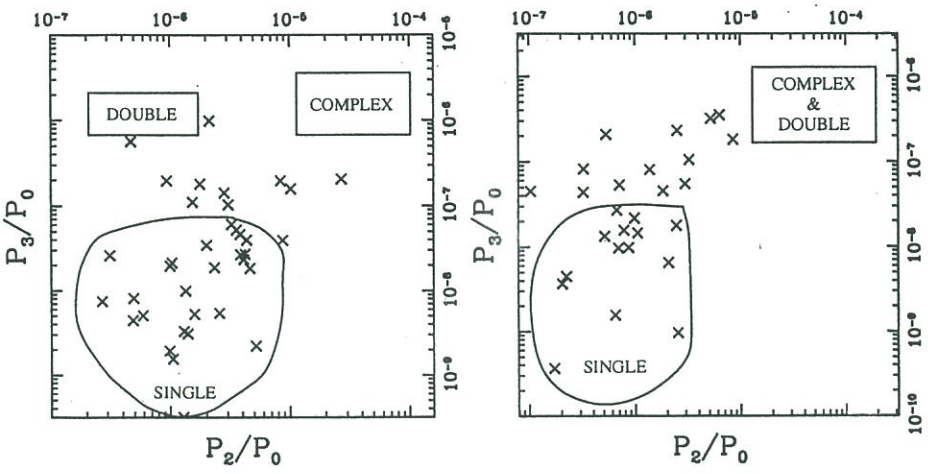

Figure 3.8. Power ratios of the brightest ~ 40 clusters (Buote & Tsai 1996) computed within apertures of 0.5 Mpc (Left) and 1 Mpc (Right).

obtained from *ASCA* data depending on the PSF deconvolution procedure used (see White 2000; Irwin & Bregman 2000 and references therein) the detailed temperature features obtained with *ASCA* do need to be confirmed with *Chandra* and *XMM* (as do those with *BeppoSAX* because of its low spatial resolution.) Nevertheless, the overall trend of non-azimuthal temperature structures and the shock-heating of the intra-cluster medium are supported by the available *ROSAT*, *ASCA*, and *BeppoSAX* data.

6.2. QUANTITATIVE CLASSIFICATION OF TEMPERATURE MORPHOLOGY

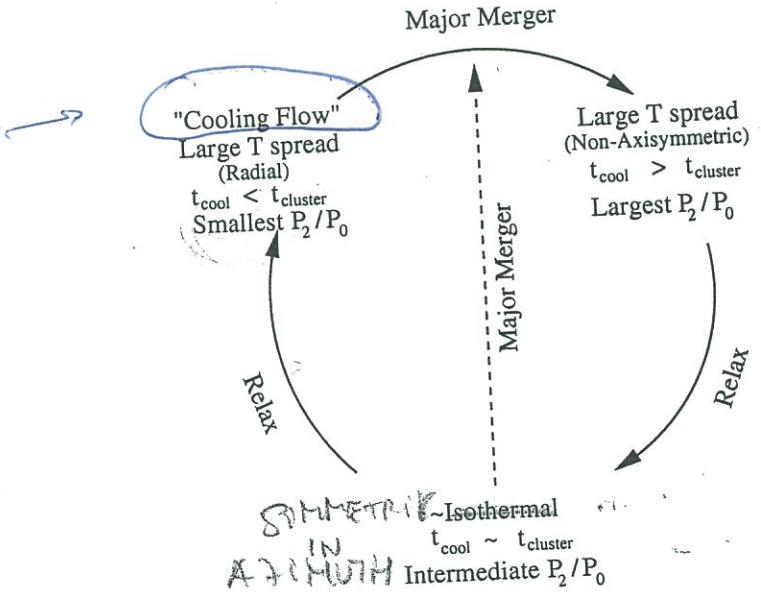

Figure 3.17. A possible description of the evolution of the X-ray temperature structure and image morphology during the formation and evolution of a cluster.

To obtain a more complete picture of the current dynamical states and the merger histories of clusters the global morphological classification of cluster images discussed in § 2 should also incorporate the morphologies of X-ray temperature maps. In Figure 3.17 I show an idealized picture of how the temperature morphology of a cluster might evolve during a merger. At early times there is a large spread of temperatures dis-

AN X-RAY TEMPERATURE MAP OF COMA

ULRICH G. BRIEL
Max-Planck-Institut für extraterrestrische Physik,
85740 Garching, Germany
E-mail: ugb@mpe-garching.mpg.de

J. PATRICK HENRY
Institute for Astronomy, University of Hawaii,
Honolulu, HI 96822, USA
E-mail: henry@uhifa.ifa.hawaii.edu

We present an X-ray temperature map of the Coma cluster of galaxies obtained with the ROSAT PSPC. As expected from the X-ray surface brightness distribution the intracluster gas of Coma is not isothermal. The temperature structure resembles a bow shock of hot gas produced by the passage of the subcluster around NGC 4839 through the main cluster, confirming hydrodynamical simulations.

1 Introduction

The Coma cluster of galaxies was long considered to be the archtype of a relaxed virialized cluster in a state of dynamical equilibrium (c.f. Kent and Gunn[1]). There were however conflicting claims that Coma shows substructure, seen as a clumping of galaxies around the brightest galaxies in the cluster (c.f. Baier[2], Fitchett and Webster[3], and Mellier *et al.*[4]). On the other hand, Geller and Beers[5] and Dressler and Schectman[6] claim that there is no statistically significant structure in the Coma cluster. The first unequivocal evidence for substructure in Coma came from an X-ray image, obtained during the all sky survey of the ROSAT satellite (Briel, Henry and Böhringer[7]). They found diffuse X-ray emission from the regions of the NGC 4839 and 4911 subgroups and interpreted the 4839 group to be in the process of merging with the main cluster. Long ROSAT PSPC pointed observations revealed even more irregular cluster structure and X-ray emission from a number of bright galaxies (White, Briel and Henry[8] and Dow and White[9]). Applying the wavelet transform analysis to these pointed observations, more significant substructure was found in the core of Coma (c.f. Biviano *et al.*[10] and Vikhlinin, Forman and Jones[11]). Using these observational results, Burns *et al.*[12] made hydrodynamic/N-body simulations and concluded that the 4839 group has already passed through the Coma cluster. More evidence for the merging scenario came from the first temperature map of the intracluster gas of Coma, obtained from the ASCA observation (Honda *et al.*[13]) and from further simulations by Ishizaka and

Table 1: Journal of Observations.

Date	RA (2000) h min sec	DEC (2000) ^{o} ' "	Exposure (ksec) MV $\leq$ 170
1991 Jun 16	12 57 43.20	+27 36 00.0	20.3
1991 Jun 16 – Jun 17	12 59 45.60	+27 48 00.0	21.5
1991 Jun 17 – Jun 18	12 59 45.60	+27 58 12.0	20.8
1991 Jun 18 – Jun 19	13 00 31.20	+28 07 48.0	21.2

Mineshige [14].

In this paper we report on a more detailed temperature map of Coma, obtained from the pointed ROSAT PSPC observations. Although ROSAT only observes in an energy band from 0.2 to 2.5 keV, we have shown on several clusters of galaxies that it is possibile to determine the usual high cluster temperatures, given a sufficiently high photon statistic (c.f. Briel and Henry [15] and Henry and Briel [16]).

2 Observations and Data Reduction

The Coma cluster was in the field of view of 4 pointed observations performed with the PSPC (Pfeffermann *et al.* [17]) on board the ROSAT satellite (Trümper [18]). In Table 1 we show the journal of the observations with the pointing directions and the accepted on axis exposure times. A spatial analysis was done by White, Briel and Henry [8] from which we show in Figure 1 the surface brightness distribution in the 0.5 – 2.4 keV energy band. To emphasize faint structures they used an increasingly large smoothing at increasing lower surface brightness. For more details on the procedure and on the interpretation of the image see references 8 and 9.

To obtain a temperature map of the intra cluster gas, we used essentially the same procedure we have described in detail in the paper about the temperature map of A2142 (Henry and Briel [19]). The main difference was that for Coma we used the Rev2 data of the SASS, using the EXSAS command *process/ct* to correct for spatial variations of the PSPC gain and to adjust the overall gain of the PSPC within 33 arcmin diameter to a value consistent with the temperature of 8.11 $\pm$ 0.04 keV, as measured with the GINGA satellite (David *et al.* [20]). The neccessay adjustment of the gain was in the order of $\pm$1% for the four observations. Background-subtracted spectra from sectors of rings centered near the center of Coma from each pointing were summed, after correcting each photon for vignetting, and then fitted to Raymond–Smith models with the heavy-element abundance fixed to 0.22 of their solar values.

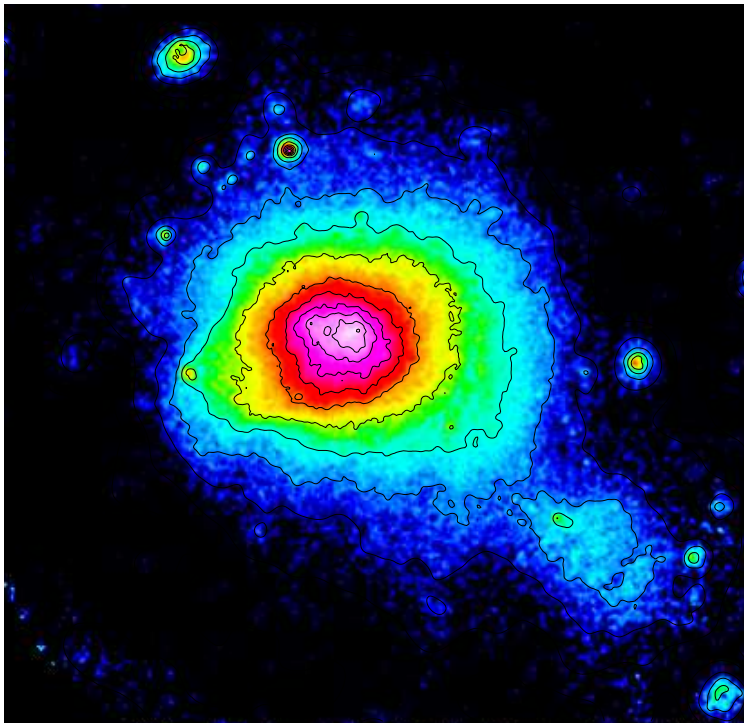

Figure 1: False color image of the surface brightness distribution of Coma in the 0.5 – 2.4 keV band with overlain contours. The contour levels are 0.125,0.25,0.5,1,2,4,8,12,16,20,24,28$\times 10^{-4}$counts sec^{-1} (16 arcsec$\times$16 arcsec)$^{-1}$, including a background of $\approx$ 0.1 in the same units. (Some of the lower contours are not visible).

As usual, photons from point sources were excluded during all spectral fits. Special care was taken to obtain the background level outside at least 50 arcmin from the cluster center, at which Coma shows a surface brightness of less then 0.3% from its peak brightness, which is less than 20% of the background. In Figure 2 we show the result of the spectral fitting of the different regions as a color representation of the temperatures with overlain contour map of the surface brightness from Figure 1. The four temperature bands are roughly separated by $\approx$ 1 σ (for one parameter of interest). There are three main points to note: (1) The region around NGC 4839 shows a low temperature of 4.8 +1.1/-0.8 keV, consistent with the typical temperature of a group of galaxies. (2) There is a hot arc-shaped region at the west side of the cluster

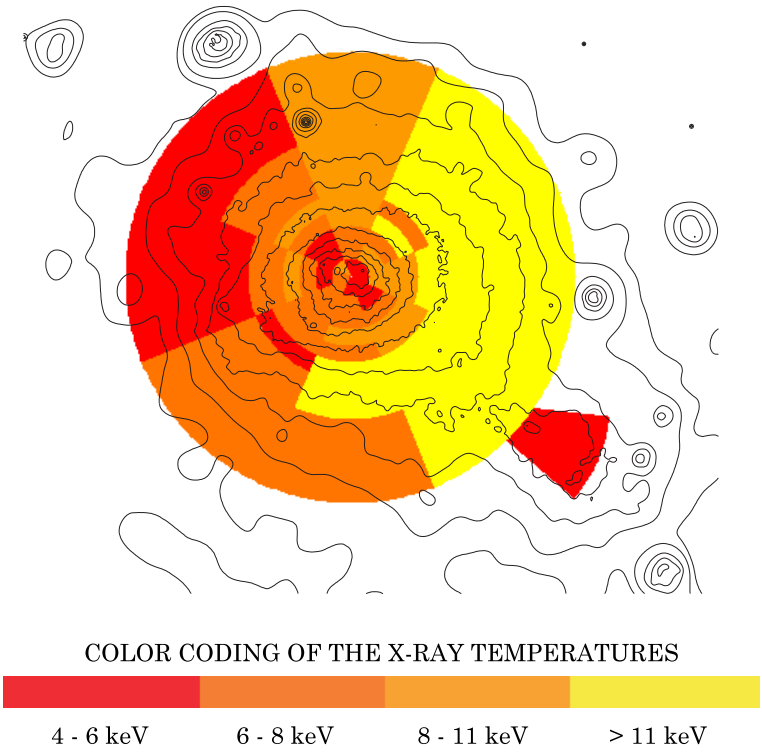

Figure 2: Color–coded temperature map of Coma with superposed surface brightness contours in the 0.5 – 2.4 keV band. The contour levels are the same as in Figure 1.

where the NGC 4839 group is located, confirming the result of the ASCA measurement [13]. (3) Within 30 arcmin diameter, where the cluster has its highest surface brightness, we find significant temperature structure on scales of a few arcmin (1 arcmin corresponds to 40 h_{50}^{-1} kpc).

3 Conclusions

The intracluster gas of the Coma cluster of galaxies shows significant temperature structure on large scales and down to a few arcmin scale. The large scale temperature structure resembles an arc-shaped bow shock at a significant

higher temperature compared with the rest of the cluster, located at the same side where the cooler galaxy group around NGC 4839 is found. This bow shock can be interpreted as the result of the passage of the group through the main cluster, as it was suggested by hydrodynamic/N-body simulations of merger events [12, 14]. Hence, this temperature map of the Coma cluster of galaxies might have answered the open question whether the subgroup is on its way through the cluster or if it already has passed the cluster core. If the answer is in fact in favor of the post-merger scenario, then an other puzzle occurs: where does the intragroup gas come from? Was there enough time after the passing to built up new gas, or was the stripping of the group gas while passing through the cluster inefficient? More simulations of the merging/passing of a group with/through a cluster are needed to clarify those questions.

Acknowledgements

The ROSAT project is supported by the BMBF. JPH thanks Prof. J. Trümper and the ROSAT group for their hospitality during the course of this research. JPH was supported by NASA grant NAG5-1789, and NATO grant CRG 910415. UGB and JPH thank Simon White for using his Coma Rev2-data prior to the release into the public archive.

References

1. Kent, S.M. and Gunn, J.E. *Astron. Journal* **87**, 945 (1982).
2. Baier, F.W. *Astr. Nach.* **305**, 175 (1984).
3. Fitchett, M., and Webster, R. *Astroph. Journal* **317**, 653 (1987).
4. Mellier, Y., Mathez, G., Mazure, A., *et al. A&A* **199**, 67 (1988).
5. Geller, M.J., and Beers, T.C. *Pub. A.S.P.* **94**, 421 (1982).
6. Dressler, A. and Schectman, S. *Astron. Journal* **95**, 985 (1988).
7. Briel, U.G., Henry, J.P. and Böhringer, H. *A&A* **259**, L31 (1992).
8. White, S.D.M., Briel, U.G. and Henry, J.P. *MNRAS* **261**, L8 (1993).
9. Dow K.L. and White, S.D.M. *Astroph. Journal* **439**, 113 (1995).
10. Biviano, A., Durret, F., Gerbal, D. *et al. Astron. and Astroph.* **311**, 95 (1996).
11. Vikhlinin, A., Forman W. and Jones, Ch. *Astroph. Journal* **435**, 162 (1995).
12. Burns, J., Roettiger, K., Ledlow, M., *et al. Astroph. Journal* **427**, L87 (1994).
13. Honda, H., Hirayama, M., Watanabe, M., *et al. ApJ* **473**, L71 (1996).
14. Ishizaka,C. and Mineshige, S. *Publ. Astron. Soc. Japan* **48**, L37 (1996).
15. Briel, U.G. and Henry, J.P. *Nature* **372**, 439 (1994).
16. Henry, J.P. and Briel, U.G. *Astroph. Journal* **433**, L9 (1995).
17. Pfeffermann, E., Briel, U. G., Hippmann, H., *et al. SPIE* **733**, 519 (1986).
18. Trümper, J. *Adv. Space Res.* **2(4)**, 241 (1983).
19. Henry, J.P. and Briel, U.G. *Astroph. Journal* **472**, 137 (1996).
20. David, L.P., Slyz, A., Jones, Ch., *et al. Astroph. Journal* **412**, 479 (1993).

A&A 521, A78 (2010)
DOI: 10.1051/0004-6361/201014839

Astronomy & Astrophysics

The complex structure of Abell 2345: a galaxy cluster with non-symmetric radio relics⋆

W. Boschin[1], R. Barrena[2,3,4], and M. Girardi[4,5]

[1] Fundación Galileo Galilei - INAF, Rambla José Ana Fernández Perez 7, 38712 Breña Baja (La Palma), Canary Islands, Spain
e-mail: boschin@tng.iac.es
[2] Instituto de Astrofísica de Canarias, C/vía Láctea s/n, 38205 La Laguna (Tenerife), Canary Islands, Spain
[3] Departamento de Astrofísica, Universidad de La Laguna, Av. del Astrofísico Francisco Sánchez s/n, 38205 La Laguna (Tenerife), Canary Islands, Spain
[4] Dipartimento di Fisica dell'Università degli Studi di Trieste, Sezione di Astronomia, via Tiepolo 11, 34143 Trieste, Italy
[5] INAF – Osservatorio Astronomico di Trieste, via Tiepolo 11, 34143 Trieste, Italy

Received 21 April 2010 / Accepted 4 June 2010

ABSTRACT

Context. The connection of cluster mergers with the presence of extended, diffuse radio sources in galaxy clusters is still debated.
Aims. We aim to obtain new insights into the internal dynamics of the cluster Abell 2345. This cluster exhibits two non-symmetric radio relics well studied through recent, deep radio data.
Methods. Our analysis is based on redshift data for 125 galaxies acquired at the Telescopio Nazionale Galileo and on new photometric data acquired at the Isaac Newton Telescope. We also use ROSAT/HRI archival X-ray data. We combine galaxy velocities and positions to select 98 cluster galaxies and analyze the internal dynamics of the cluster.
Results. We estimate a mean redshift $\langle z \rangle = 0.1789$ and a line-of-sight (LOS) velocity dispersion $\sigma_V \sim 1070$ km s^{-1}. The two-dimensional galaxy distribution reveals the presence of three significant peaks within a region of $\sim 1\ h_{70}^{-1}$ Mpc (the E, NW, and SW peaks). The spectroscopic catalog confirms the presence of these three clumps. The SW and NW clumps have similar mean velocities, while the E clump has a larger mean velocity ($\Delta V_{\rm rf} \sim 800$ km s^{-1}); this structure causes the presence of the two peaks we find in the cluster velocity distribution. The difficulty in separating the galaxy clumps leads to a very uncertain mass estimate $M \sim 2 \times 10^{15}\ h_{70}^{-1}\ M_{\odot}$. Moreover, the E clump well coincides with the main mass peak as recovered from the weak gravitational lensing analysis and is off-set to the east from the BCG by $\sim 1.3'$. The ROSAT X-ray data also show a very complex structure, mainly elongated in the E-W direction, with two (likely three) peaks in the surface brightness distribution, which, however, are off-set from the position of the peaks in the galaxy density. The observed phenomenology agrees with the hypothesis that we are looking at a complex cluster merger occurring along two directions: a major merger along the ~E-W direction (having a component along the LOS) and a minor merger in the western cluster regions along the ~N-S direction, roughly parallel to the plane of the sky. The eastern radio relic is elongated in the direction perpendicular to that of the major merger, while the peculiar, western radio relic is elongated in the direction perpendicular to the bisecting of the two merger directions.
Conclusions. Our scenario for the internal dynamics of Abell 2345 strongly supports the use of the "outgoing merger shocks" model to explain the two radio relics, suggesting a consistent justification for their asymmetry.

Key words. galaxies: clusters: individual: Abell 2345 – galaxies: clusters: general – galaxies: distances and redshifts

1. Introduction

Diffuse radio emission in galaxy systems is a rare phenomenon presently known in only a few tens of (mostly) rich clusters (e.g. Giovannini et al. 1999; see also Giovannini & Feretti 2002; Feretti 2005; Giovannini et al. 2009). These radio sources (named halos and relics) are very interesting for their possible connection with cluster mergers (see Feretti et al. 2002, for a review). They show a typical synchrotron spectrum, a clear sign of the existence of large-scale cluster magnetic fields and of widespread relativistic particles. Cluster mergers have been suggested to provide the large amount of energy necessary for electron reacceleration up to relativistic energies and for magnetic field amplification (Feretti 1999, 2002; Sarazin 2002). Radio relics ("radio gischts" as referred by Kempner et al. 2003), which are polarized and elongated radio sources located in the cluster peripheral regions, seem to be directly associated with merger shocks (e.g., Ensslin et al. 1998; Roettiger et al. 1999; Ensslin & Gopal-Krishna 2001; Hoeft et al. 2004). Radio halos, unpolarized sources which permeate the cluster volume similarly to the X-ray emitting gas, are more likely to be associated with the turbulence following a cluster merger (Cassano & Brunetti 2005). However, only recently the number of diffuse radio sources discovered in clusters has grown enough to allow their study on the basis of a sufficient statistics and to attempt a classification (e.g. Kempner et al. 2003; Ferrari et al. 2008).

There is growing evidence of the connection between diffuse radio emission and cluster mergers based on X-ray data (see Buote 2002; Feretti 2006, 2008 and references therein). Optical data are a powerful way to investigate the presence and the dynamics of cluster mergers (e.g., Girardi & Biviano 2002), too. The spatial and kinematical analysis of member galaxies allow us to detect and measure the amount of substructure, to identify and analyze possible pre-merging clumps or merger remnants.

⋆ Table 1 is only available in electronic form at http://www.aanda.org

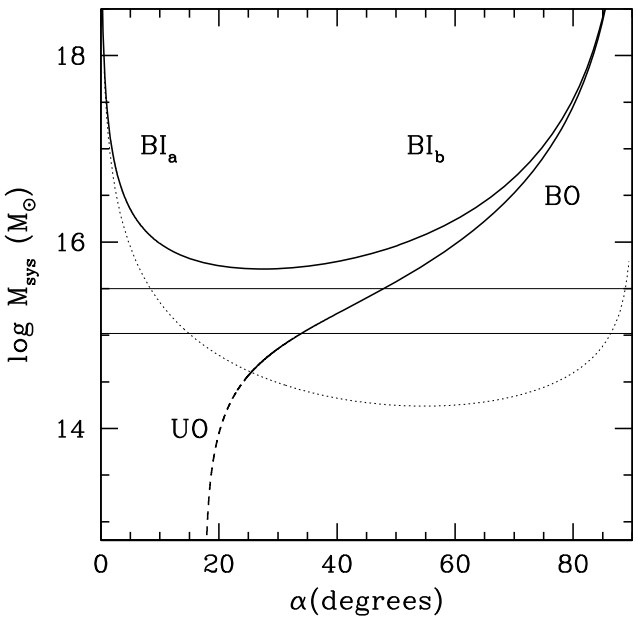

Fig. 10. System mass vs. projection angle for bound and unbound solutions (thick solid and thick dashed curves, respectively) of the two-body model applied to the E and SN+SW subsystems. Labels BI_a and BI_b indicate the bound and incoming, i.e., collapsing solutions (thick solid curve). Label BO indicates the bound outgoing, i.e., expanding solutions (thick solid curve). Label UO indicates the unbound outgoing solutions (thick dashed curve). The horizontal lines give the range of observational values of the mass system with a 50% error. The thin dashed curve separates bound and unbound regions according to the Newtonian criterion (above and below the thin dashed curve, respectively).

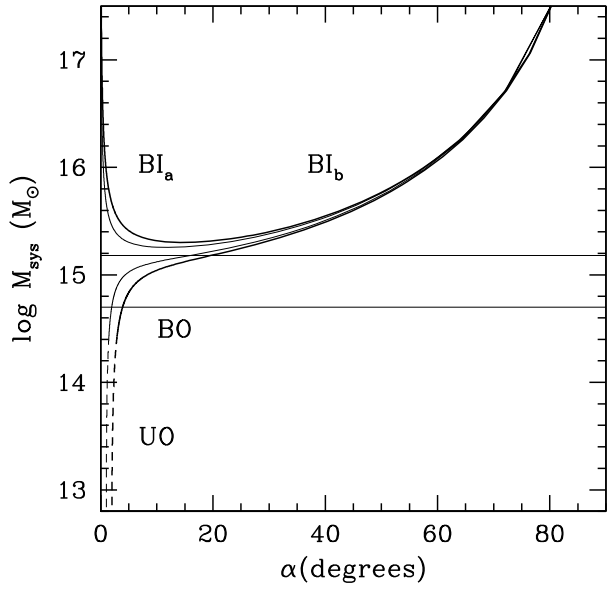

Fig. 11. The same that in Fig. 10 but for the NW and SW subsystems. Thick and thin lines give the results for $V_{rf,LOS} \sim 100$ and 50 km s^{-1}, respectively.

of the shock $\mathcal{M} \sim 2.8$ as inferred by B09 from the radio spectral index of A2345–2. The Mach number is defined to be $\mathcal{M} = v_s/c_s$, where v_s is the velocity of the shock and c_s is the sound speed in the pre-shock gas (see e.g., Sarazin 2002 for a review). The value of c_s, obtained from our estimate of $\sigma_{V,E} \sim 900$ km s^{-1}, leads to a value of $v_s \sim 2.5\times10^3$ km s^{-1}. Assuming the shock velocity to be a constant, the shock covered a $\sim 0.9\ h_{70}^{-1}$ Mpc scale (i.e., the distance of the relic from the cluster center) in a time of ~0.35 Gyr. We assume this time as our estimate of t. Although the velocity of the shock is not constant, studies based on numerical simulations show how the variation in v_s is much smaller than the variation in the relative velocity of the subclumps identified with their dark matter components (see Fig. 4 of Springel & Farrar 2007, and Fig. 14 of Mastropietro & Burkert 2008), thus our rough estimate of t is acceptable as a first order approximation.

The bimodal model solution gives the total system mass M_{sys}, i.e. the sum of the masses of the E+SW+NW groups, as a function of α, where α is the projection angle between the plane of the sky and the line connecting the centers of the two clumps (e.g., Gregory & Thompson 1984). Figure 10 compares the bimodal-model solutions with the observed mass of the system considering a 50% uncertainty band. The present solutions span the bound outgoing solutions (i.e., expanding), BO; the bound incoming solutions (i.e., collapsing), BI_a and BI_b; and the unbound outgoing solutions, UO. For the incoming case, there are two solutions because of the ambiguity in the projection angle α. The BO solution is the only one to be consistent with the observed mass range leading to a $\alpha \sim 40$–50 degrees. The BO solution means that the E group is moving towards East going in the opposite direction with respect to the observer, while the SW+NW complex is moving toward West toward the observer. The angle estimate means that the true spatial distance between the two subclumps is ~1.3–1.5 h_{70}^{-1} Mpc and that the real, i.e. deprojected, velocity difference is $V_{rf} \sim 1000$–1250 km s^{-1}. We note that the present relative velocity between galaxy clumps is smaller than the shock velocity, i.e., the regime is not stationary, but this is expected when comparing shock and collisionless components in numerical simulations (Springel & Farrar 2007; Mastropietro & Burkert 2008). The deprojected velocity difference of the two clumps at the cross core time is $V_{rf} \sim 2000$–2800 km s^{-1}, i.e. comparable to that of the shock as expected.

As for the second collision, the values of relevant parameters for the two-clump system (the SW and the NW groups) are $V_{rf} \sim 0$ km s^{-1} (since we do not see any significant velocity difference), $D \sim 0.3\ h_{70}^{-1}$ Mpc and $M_{sys} \sim 1.1 + 0.5 \sim 1.6 \times10^{15}\ h_{70}^{-1}\ M_\odot$. In our scenario this merger is more recent than the above one and thus we assume a time $t \sim 0.2$ Gyr.

Figure 11 shows the results for $V_{rf} = 50$ km s^{-1} and $V_{rf} = 100$ km s^{-1}. The BO solution is well acceptable with $\alpha \sim 2$–20°. This means that the SW group is moving toward South and the NW group towards North and, as someway expected from the observations, the NW and SW groups define a direction almost parallel to the plane of the sky. The true spatial distance is similar to the projected one. The real velocity difference has a huge uncertainty due to its dependence from the very uncertain α value. Notice that this merger should be considered of minor importance with respect to the main one described above, thus here the bimodal model is likely a worse representation of the reality than the above case.

In conclusion, we recover from our toy model quantitative results consistent with the global scenario. Thus, our analysis of the internal cluster dynamics well supports the "outgoing merger shocks" model proposed by B09. We also present an explanation for the relics asymmetry and the peculiarity of A2345–1. Our explanation is based on the internal structure of A2345, rather than on a possible merger with an external, close group (e.g. the group "X1" detected by B09). Before applying more reliable approaches to the study of A2345 internal dynamics, an improvement of the present observational picture would be very useful,

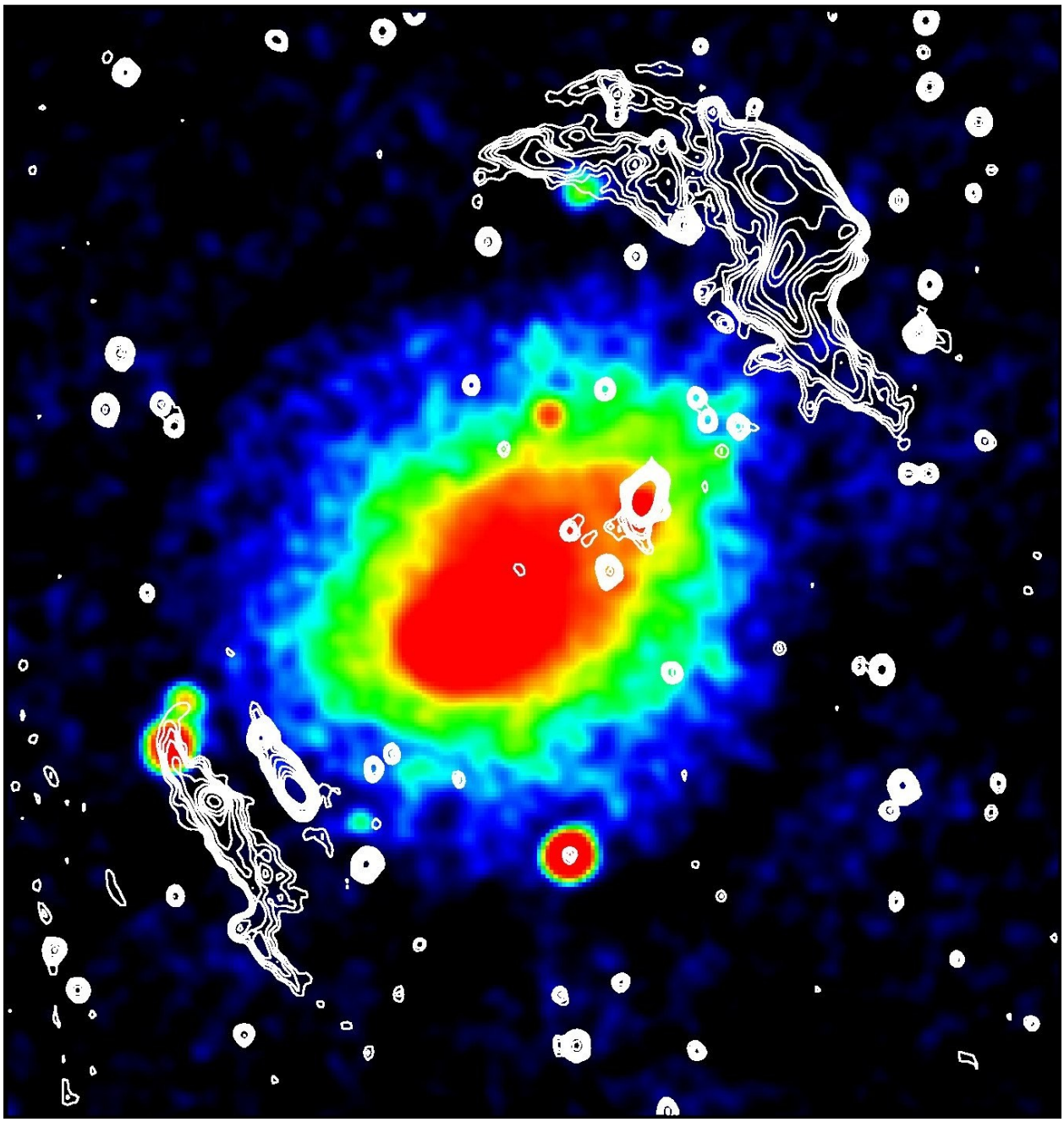

Although others have suggested that A3667 has recently undergone a merger (Knopp et al. 1996), and still others have suggested a possible shock origin for the extended radio emission (Röttgering et al. 1997; Ensslin et al. 1998), this is the first study that presents a quantitative numerical model that attempts to simultaneously explain the radio, optical, and X-ray morphology of this cluster within the context of a single merger.

Section 2 is a review of recent observations and evidence for substructure in A3667. In § 3 we discuss our numerical method. Our initial conditions are presented in § 4. Section 5 summarizes our model constraints. We discuss the radio halo model and its limitations in § 6. Finally, we summarize our results in § 7. The model is scaled assuming $H_0 = 70$ km s^{-1} Mpc^{-1}. The observational data (see § 2) are parameterized by $h = H_0/100$.

2. A REVIEW OF THE OBSERVATIONS

2.1. *The X-Ray Data*

Knopp et al. (1996) provide a detailed analysis of the *ROSAT* X-ray data that we summarize here. The X-ray surface brightness (XSB; *contours*, Fig. 1) is seen to be elongated from the southeast to the northwest. The ellipticity is greatest in the cluster core and decreases with increasing radius. There is an isophotal twisting of $\sim 15°$ from the inner to the outer cluster. The XSB exhibits an extension to the northwest of the core while it is seen to be flattened to the southeast. This results in a significant centroid shift (Mohr et al. 1995). A3667 does not appear to be isothermal. Knopp et al. (1996) find a mean temperature of $6.3^{+0.5}_{-0.6}$ keV. However, the core is found to be hotter ($9^{+4.0}_{-2.0}$ keV) than the mean at the 82% confidence level. Markevitch et al. (1998), using *ASCA* data, find a mean temperature of 7.0 ± 0.6 keV. They do not, however, observe the elevated core temperature seen in the *ROSAT* data. This issue can be addressed with *AXAF*. Using the *ROSAT*-derived XSB, Knopp et al. (1996) find the total X-ray luminosity within 0.80 h^{-1} Mpc to be $L_X = (6.74 \pm 0.09) \times 10^{44}\ h^{-2}$ ergs s^{-1}. They estimate the gas mass within 0.80 h^{-1} Mpc to be $(8.9 \pm 0.9) \times 10^{12}\ h^{-5/2}\ M_\odot$ while the total dynamical mass within the same radius (assuming hydrostatic equilibrium, which is questionable in a recent merger) is $3.5^{+0.3}_{-0.4} \times 10^{14}\ h^{-1}\ M_\odot$, giving a relatively low baryon fraction of 2.5 $h^{-3/2}$%. The total mass within 3.0 h^{-1} Mpc is estimated to be $(1.4 \pm 0.2) \times 10^{15}\ h^{-1}\ M_\odot$.

2.2. *The Optical Data*

Sodré et al. (1992) provide 203 galaxy positions (128 redshifts) in the vicinity of A3667. The mean cluster redshift is $16{,}557 \pm 117$ km s^{-1}, and the velocity dispersion is 1223^{+87}_{-72} km s^{-1}. Fadda et al. (1996), using a somewhat larger galaxy sample and an analysis of substructure, find a global velocity dispersion of 971^{+62}_{-47}, although the velocity dispersion in the core appears to be much higher. Using the global velocity dispersion and the *ASCA* mean temperature, one calculates $\beta_{\rm spec} = 0.84$. This value is somewhat discrepant from the value of $\beta_{\rm fit} = 0.535$ (Knopp et al. 1996). Numerical simulations have linked the so-called β-discrepancy (Sarazin 1988) to recent merger activity (Navarro, Frenk, & White 1995; Roettiger et al. 1996). Sodré et al. (1992) further note two spatially distinct clumps within the galaxy distribution. One clump is centered on the brightest D galaxy and the XSB peak while the other is associated with the second brightest D galaxy located $\sim 16\farcm6$ to the northwest (but still within the observed XSB distribution). Figure 2 shows the positions of galaxies having redshifts supplied by Sodré et al. (1992) and the results of the δ test for substructure (Dressler & Shectman 1988). The circles, marking individual galaxy positions, are scaled in radius according to their respective δ parameter. The value of δ indicates the degree to which a galaxy and its 10 nearest neighbors deviate from the global velocity properties. In Figure 2, we have filled the circles corresponding to galaxies having the lowest δ parameters, thereby accentuating the location of the two groups noted by Sodré et al. (1992). The degree of substructure demonstrated by the δ test gives some indication as to why the observed range of velocity dispersions, and therefore cluster virial masses, is so large. Sodré et al. (1992) estimate a total mass of $2.6 \times 10^{15}\ h^{-1}\ M_\odot$ for the entire cluster while Biviano et al. (1993) find $1.6 \times 10^{15}\ h^{-1}\ M_\odot$ within 0.75 h^{-1} Mpc. Both values are larger than the X-ray–derived values (see § 2.1).

2.3. *The Radio Data*

There are many radio point sources located within the spatial extent of A3667, but for our purposes, we are concerned only with the large extended radio sources located to the southeast and northwest of the X-ray core (see Fig. 1, *gray scale*). The uniqueness of the extended radio sources in A3667 has been known for many years (Schilizzi & McAdam 1975; Goss et al. 1982; Jones & McAdam 1992). Here, we summarize the most detailed analysis to date, Röttgering et al. (1997). Approximately 1.7 h^{-1} Mpc north-

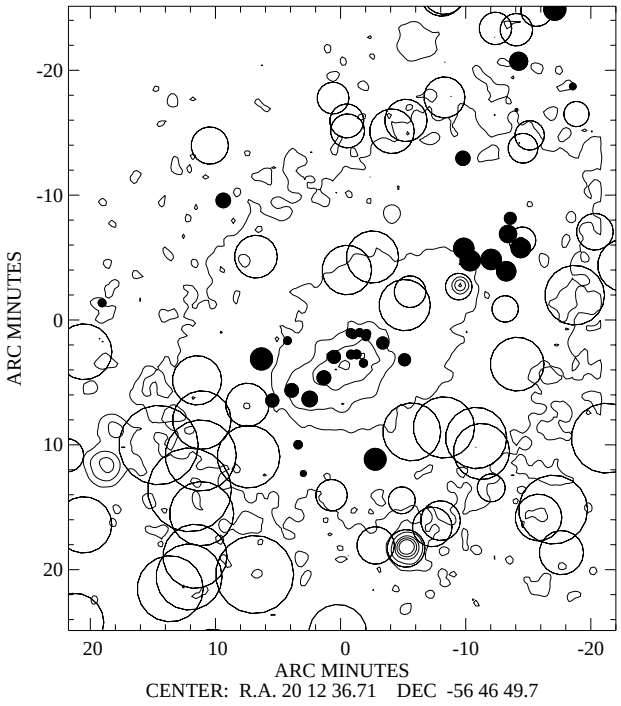

FIG. 2.—Galaxy positions (*filled and open circles*) overlaid on the *ROSAT* PSPC image (*contours*). The circle sizes are proportional to the galaxy's δ statistic (Dressler & Shectman 1988). A large value of δ indicates a large local deviation in velocity mean and dispersion from the global values. We have filled circles representing local distributions having δ less than 20% of the maximum. Note the two regions associated with the XSB peak and to the northwest of the peak. Both of these are associated with D galaxies.

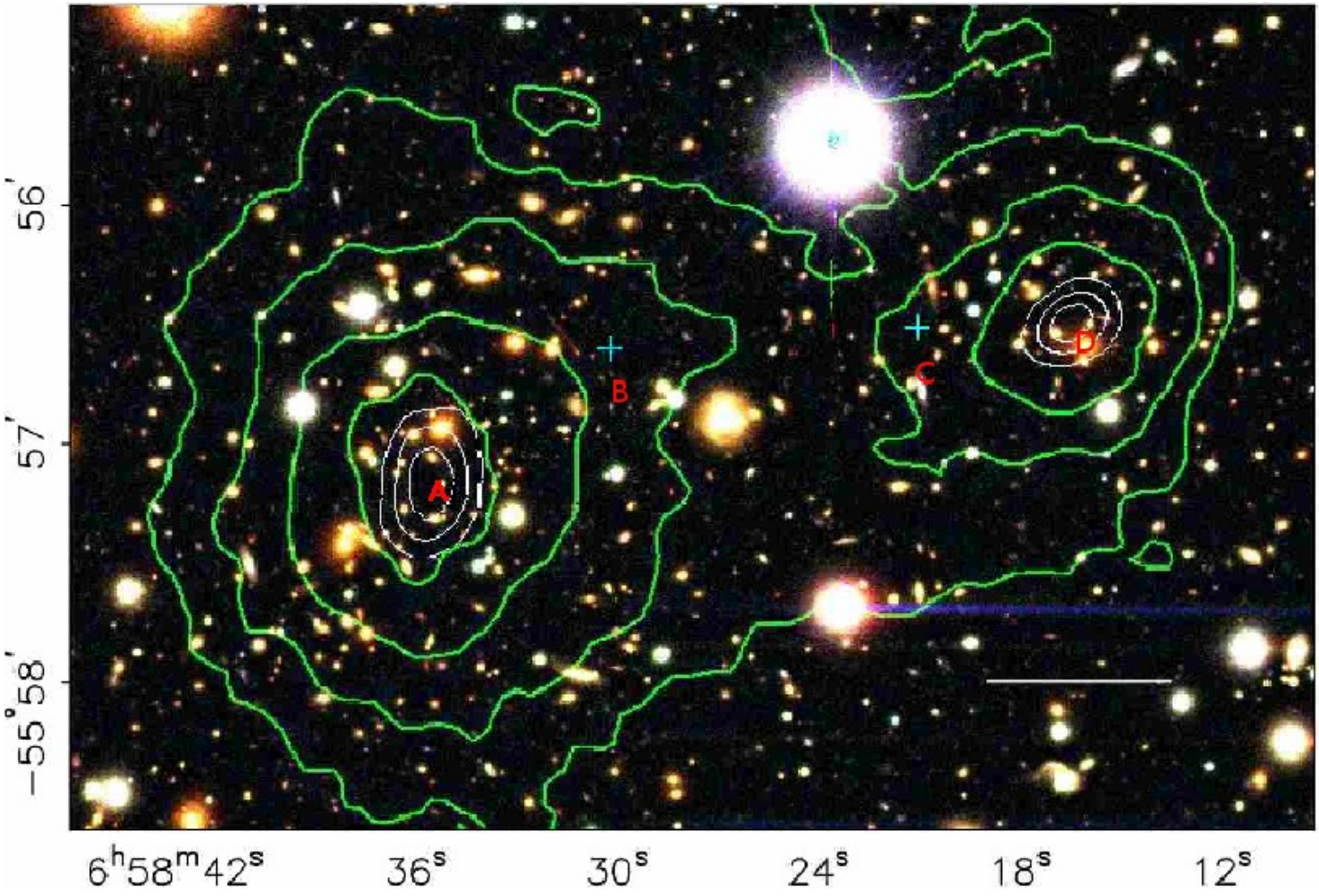
56′
57′
−55°58′
A
B
C
D
6h58m42s
36s
30s
24s
18s
12s

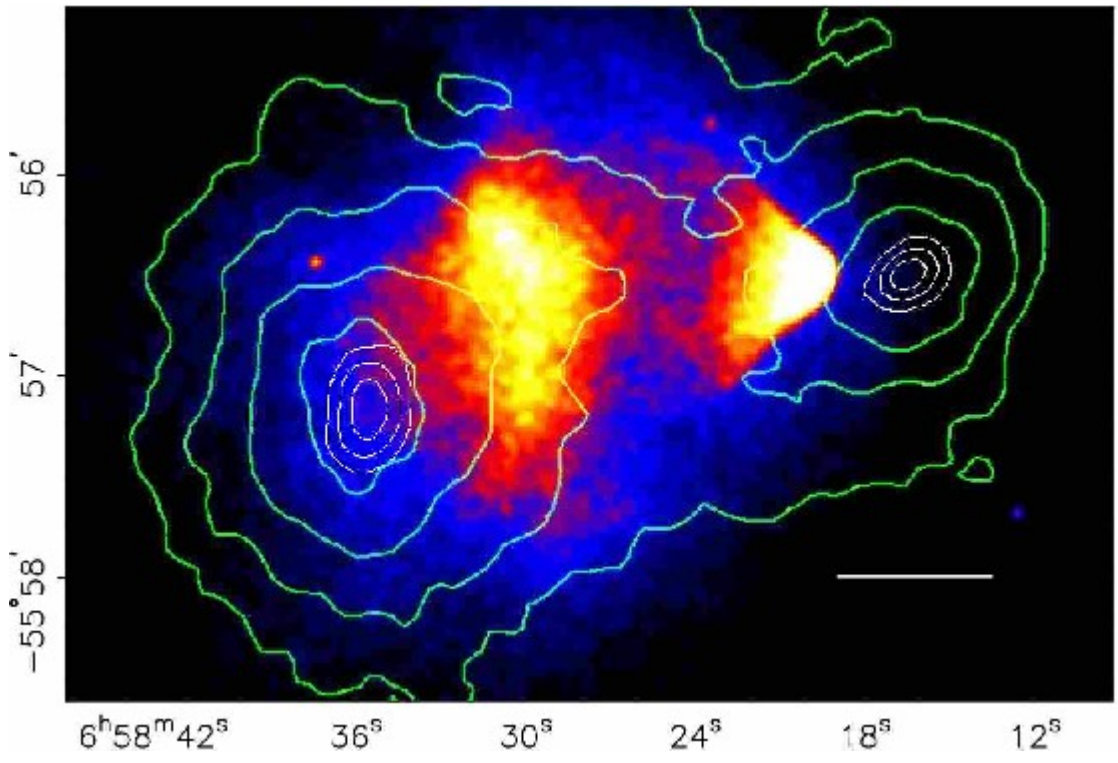
56′
57′
−55°58′
6h58m42s
36s
30s
24s
18s
12s

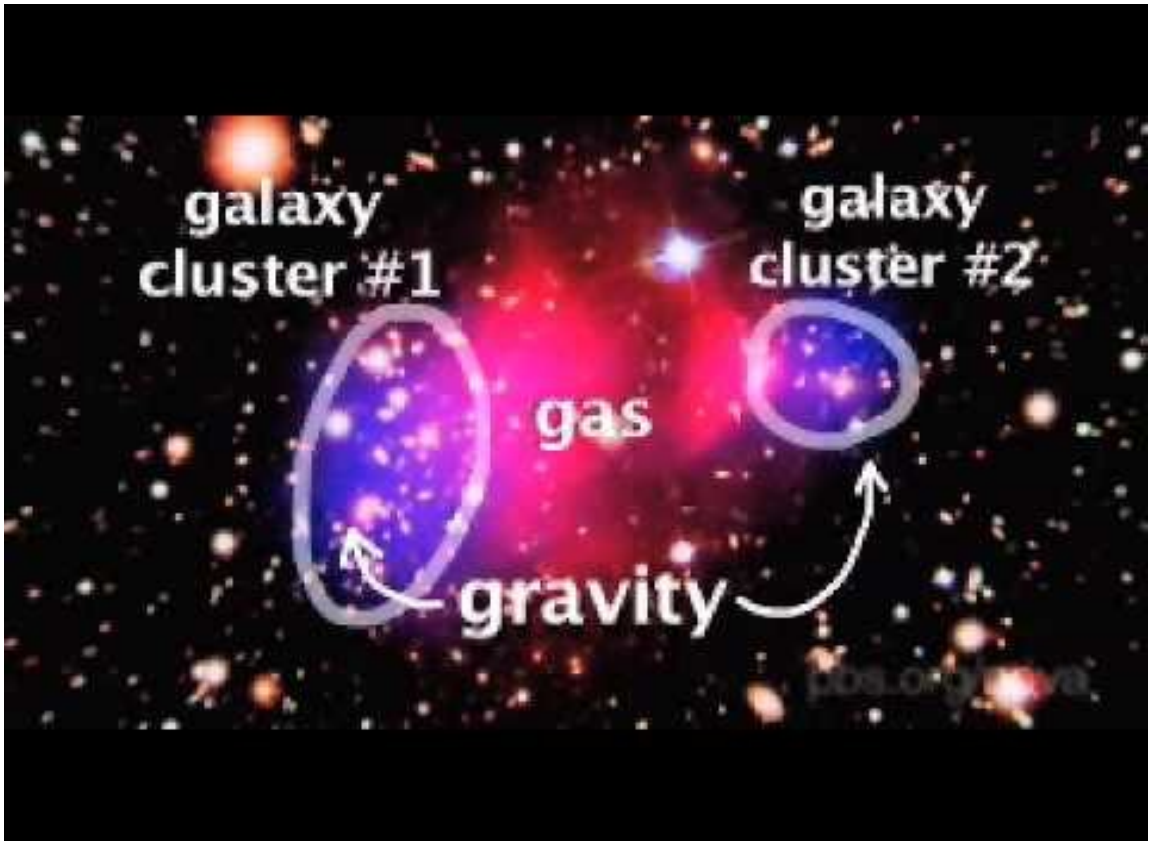
galaxy
cluster #1
galaxy
cluster #2
gas
gravity

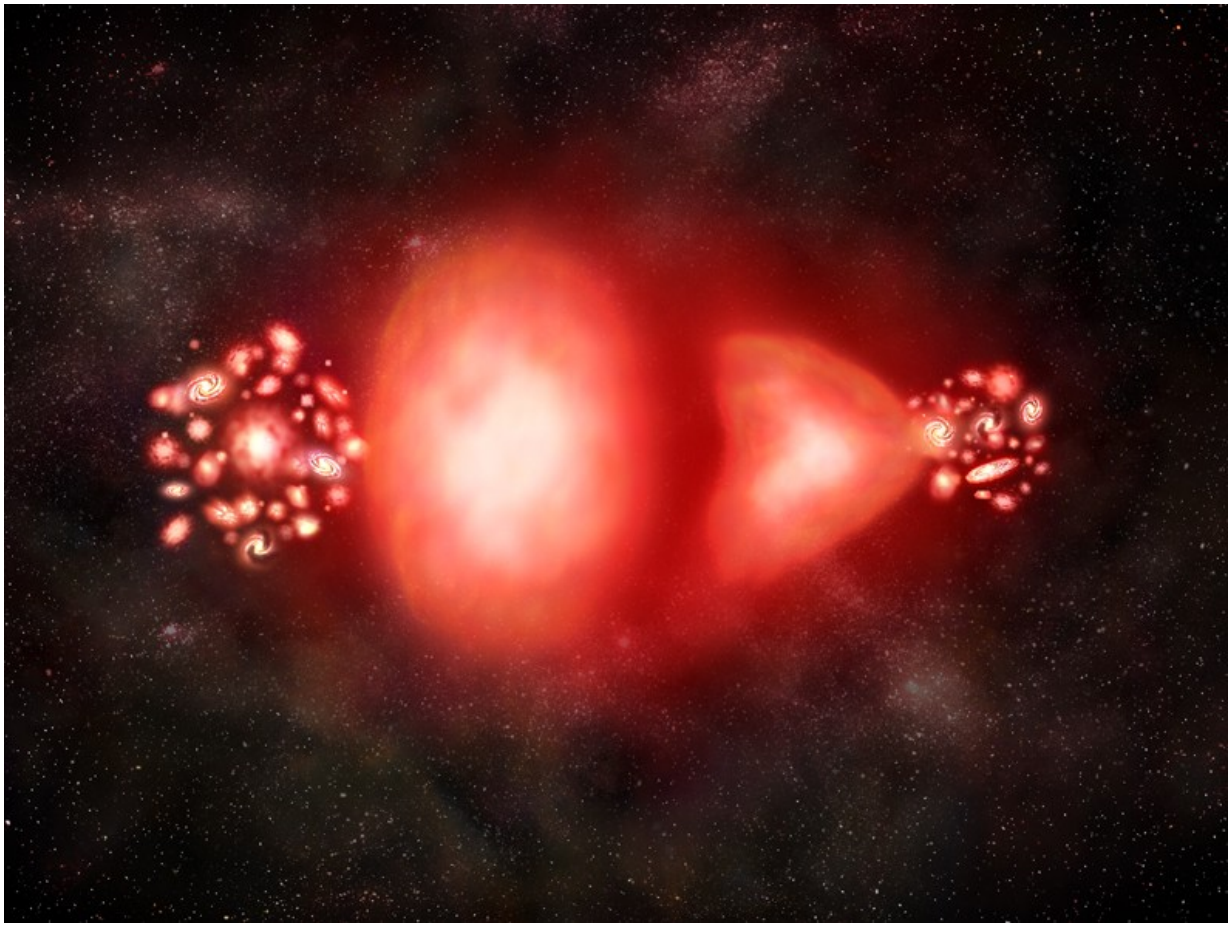

International Journal of Modern Physics D
Vol. 23, No. 4 (2014) 1430007 (76 pages)

DOI: 10.1142/S0218271814300079

COSMIC RAYS IN GALAXY CLUSTERS AND THEIR NONTHERMAL EMISSION

GIANFRANCO BRUNETTI
IRA-INAF, via P. Gobetti 101,
40129 Bologna, Italy
brunetti@ira.inaf.it

THOMAS W. JONES
School of Physics and Astronomy,
University of Minnesota,
116 Church St. SE, Minneapolis, MN 55455, USA
twj@msi.umn.edu

Received 27 December 2013
Accepted 30 December 2013
Published 3 March 2014

Radio observations prove the existence of relativistic particles and magnetic field associated with the intra-cluster-medium (ICM) through the presence of extended synchrotron emission in the form of radio halos and peripheral relics. This observational evidence has fundamental implications on the physics of the ICM. Nonthermal components in galaxy clusters are indeed unique probes of very energetic processes operating within clusters that drain gravitational and electromagnetic energy into cosmic rays (CRs) and magnetic fields. These components strongly affect the (micro-)physical properties of the ICM, including viscosity and electrical conductivities, and have also potential consequences on the evolution of clusters themselves. The nature and properties of CRs in galaxy clusters, including the origin of the observed radio emission on cluster-scales, have triggered an active theoretical debate in the last decade. Only recently we can start addressing some of the most important questions in this field, thanks to recent observational advances, both in the radio and at high energies. The properties of CRs and of cluster nonthermal emissions depend on the dynamical state of the ICM, the efficiency of particle acceleration mechanisms in the ICM and on the dynamics of these CRs. In this paper, we discuss in some detail the acceleration and transport of CRs in galaxy clusters and the most relevant observational milestones that have provided important steps on our understanding of this physics. Finally, looking forward to the possibilities from new generations of observational tools, we focus on what appear to be the most important prospects for the near future from radio and high-energy observations.

Keywords: Galaxies clusters; general radiation mechanisms; nonthermal acceleration of particles.

PACS Number(s): 95.30.Cq, 95.30.Gv, 95.30.Qd, 98.65.Cw, 98.65.Fz, 98.65.Hb

1. Introduction

Clusters of galaxies and the filaments that connect them are the largest structures in the present universe in which the gravitational force due to the matter overdensity overcomes the expansion of the universe. Massive clusters have typical total masses of the order of $10^{15} M_{\odot}$, mostly in the form of dark matter (∼70–80% of the total mass), while baryonic matter is in the form of galaxies (∼few%) and especially in the form of a hot ($T \sim 10^8$ K) and tenuous ($n_{\rm gas} \sim 10^{-1}$–$10^{-4}\,{\rm cm}^{-3}$) gas (∼15–20%), the intra-cluster-medium (ICM)[1,2] (Fig. 1). That ICM emits thermal X-rays, mostly via bremsstrahlung radiation, and also Compton-scatters the photons of the cosmic microwave background, leaving an imprint in the mm-wavelengths band that provides information complementary to the X-rays[6] (Fig. 1). In the current paradigm of structure formation, clusters are thought to form via a hierarchical sequence of mergers and accretion of smaller systems driven by dark matter that dominates the gravitational field. Mergers, the most energetic phenomena since the Big Bang,

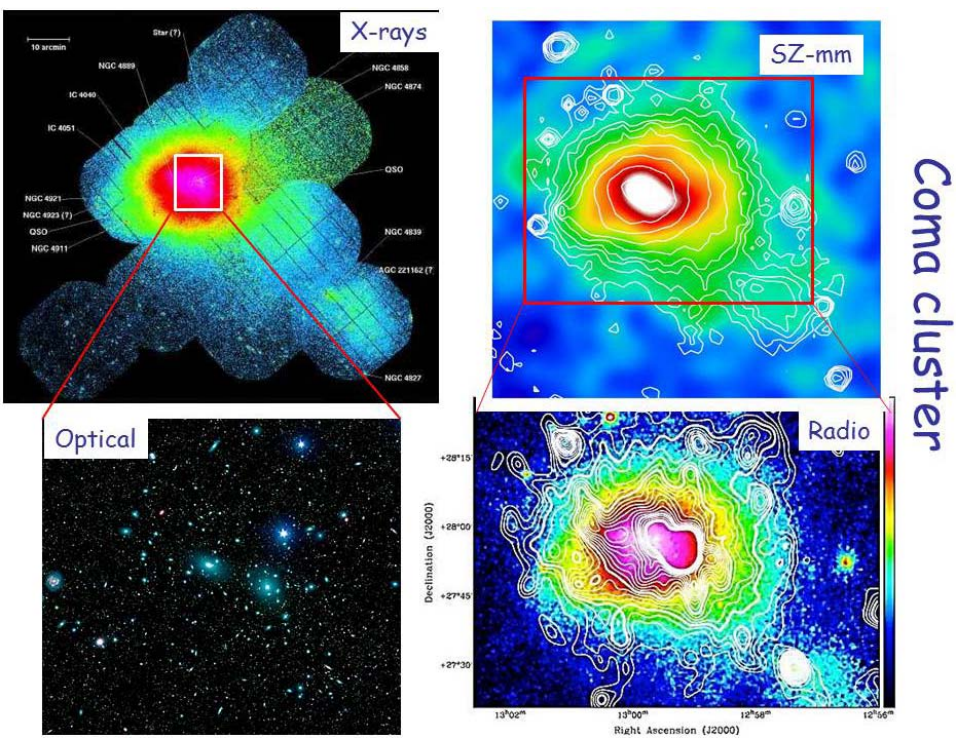

Fig. 1. Multi-frequency view of the Coma cluster: the thermal ICM emitting in the X-rays (top left, adapted from Ref. 3), the overlay between thermal SZ signal (colors) and X-rays (contours) (top right, adapted from Ref. 4), the optical emission from the galaxies in the central region of the cluster (bottom left, from Sloan Digital Sky Survey, credits NASA/JPL-Caltech/L.Jenkins (GSFC)), and the synchrotron (radio halo) radio emission (contours) overlaid on the thermal X-rays (colors) (bottom right, adapted from Ref. 5).

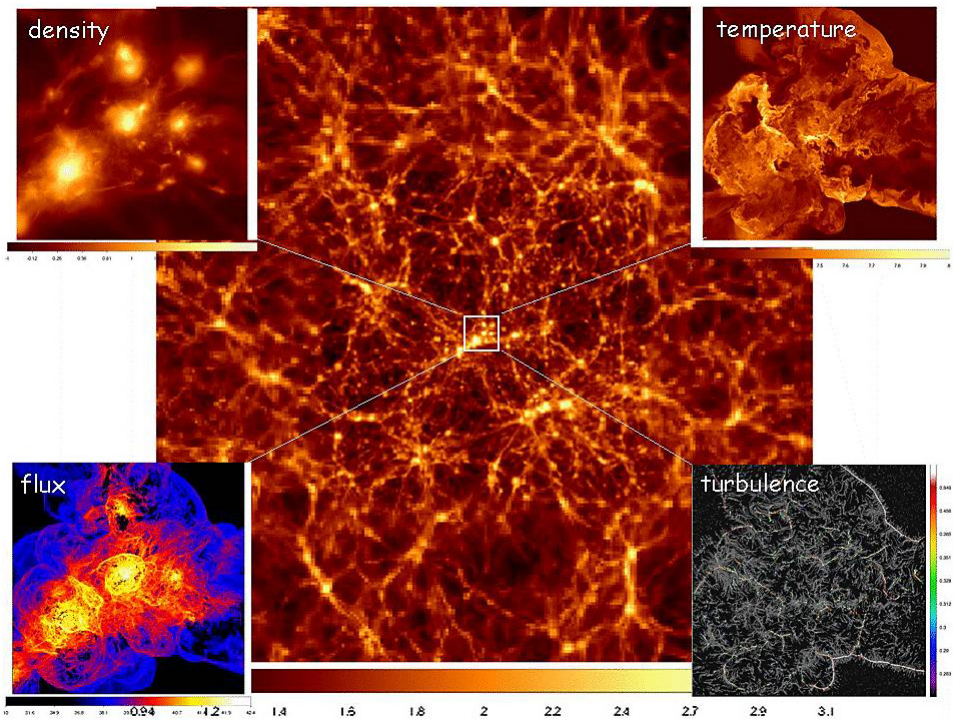

Fig. 2. Projection of matter density for a volume of size 187 Mpc/h simulated with ENZO AMR (velocity and density refinement technique) with peak spatial resolution 25 kpc/h. The two panels on the left are $8 \times 8 \times 2$ Mpc/h zooms of the central region showing the projected density (top-left) and the kinetic energy-flux (bottom-left). The two panels on the right are $8 \times 8 \times 0.025$ Mpc/h zooms of the same region showing the temperature distribution (top-right) and the overlay of shock map and turbulent velocity-vectors (obtained with a filtering of laminar motions on 300 kpc scale). Images are obtained at $z = 0.6$ from simulations presented in Ref. 79.

dissipate energy in higher density regions closer to cluster centers during mergers. Simple (analytical or semi-analytical) but accurate estimates of the amount of kinetic energy associated with accretion/external shocks are very challenging. A leap forward in understanding in this area, however, has been achieved in the last decade through extensive cosmological simulations that allow one to study the formation of shocks in clusters, from their outskirts to more internal regions with increasing detail.[13,71–73,79,81,82]

Figure 3 illustrates these points. It shows the kinetic energy flux through shock surfaces, that is, $1/2\rho V_{\rm sh}^3 S$, measured in clusters formed during cosmological simulations. Here, ρ is the upstream gas density, while $V_{\rm sh}$ and S are shock velocity and surface area, respectively. The distribution of energy fluxes shows that most of the gravitational energy is dissipated at relatively weak, "internal" (merger) shocks, with Mach number $M \sim 2$–3. A modest fraction of the kinetic energy-flux passes through related stronger internal-shocks developed during merger activity

For trans-relativistic and mildly relativistic CRp, energy losses are dominated by ionization and Coulomb scattering. CRp more energetic than the thermal electrons have[158]

$$\left(\frac{dp}{dt}\right)_i \simeq -1.7\times 10^{-29}\left(\frac{n_{\rm th}}{10^{-3}}\right)\frac{\beta_p}{\frac{3}{4}\sqrt{\pi}\beta_e^3+\beta_p^3} \quad \text{(cgs)}, \tag{24}$$

where $\beta_e = v_e/c \simeq 43\beta_p \simeq 0.18(T/10^8 K)^{1/2}$ is the RMS velocity of the thermal electrons, while β_p is the corresponding thermal proton velocity.

3.1.3. *General energy loss considerations*

Figure 8 shows the (total) time-scales for losses of CRe and CRp. CRp with energy 1 GeV–1 TeV are long-living particles with life-times in the cores of galaxy clusters $\sim$ several Gyrs. At higher energy the CRp time-scale gradually drops below 1 Gyr, while at very high energy, in the regime of ultra high energy CRp, the life-time is limited by inelastic p–γ collisions with CMB photons, as discussed in Sec. 2.2.1 (Fig. 5).

On the other hand, CRe are short-lived particles at the energies where they radiate observable emissions, due to the unavoidable radiation energy-losses (mainly ICS and synchrotron). The maximum life-time of CRe, about 1 Gyr, is at energies

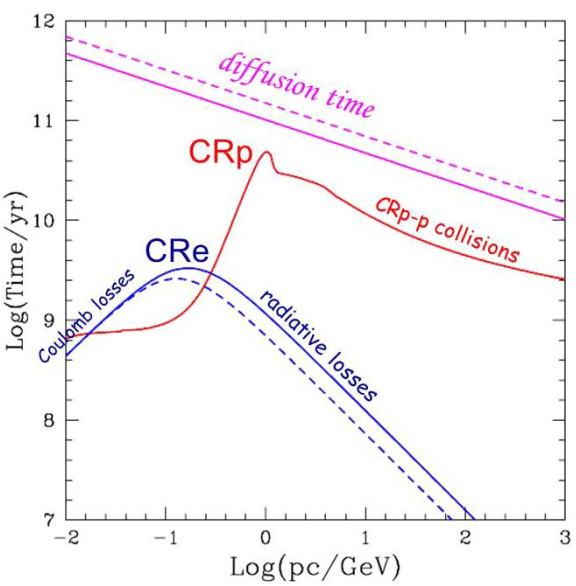

Fig. 8. (Color online) Life-time of CRp (red) and CRe (blue, lower curves) in the ICM at redshift $z = 0$, compared with the CR diffusion time on Mpc scales (magenta, upper curves) (adapted from Ref. 25). The most relevant channels of CR energy losses at different energies are highlighted in the panel. Adopted physical parameters are: $n_{\rm th} = 10^{-3}\,{\rm cm}^{-3}$, $B = 1$ (solid) and $3\,\mu$G (dashed). Diffusion is calculated assuming a Kolmogorov spectrum of magnetic fluctuations with $L_{\rm max} = 100\,{\rm kpc}$ and $f = 1$.

energy in the ICM is generated at shocks, as previously noted. Estimates of CRp acceleration efficiency suggest as much as ∼10% of the kinetic energy flux at cosmological shocks may be converted into CRs.[196] Then, one might claim that the resulting energy budget of CRs should be a substantial fraction of the ICM thermal energy. If true, the presence of the CRp could influence many aspects of ICM dynamics, including, for examples, contribution to ICM pressure support and a partial quenching of radiative cooling in core regions.

The most direct approach to constraining the energy content of CRp in ICMs consists in the searches for γ-ray emission from the decay of the neutral pions due to CRp-p collisions in the ICM. Early space-based γ-ray upper limits from EGRET observations provided limits $E_{\rm CR}/E_{\rm ICM} < 0.3$ in several nearby galaxy clusters.[26] Subsequently, more stringent limits have been derived from deep, pointed observations at energies $E_\gamma > 100\,{\rm GeV}$ with ground-based Cherenkov telescopes.[27,29,31,197–199] These limits, unfortunately, depend on the unknown spectral shape of the CRp-energy distribution and the spatial distribution of CRp in the clusters. The most stringent limits are obtained assuming $\delta = 2.1$ ($N_{CR}(p) \propto p^{-\delta}$) and a linear scaling between CRp and thermal energy densities (Fig. 10); under

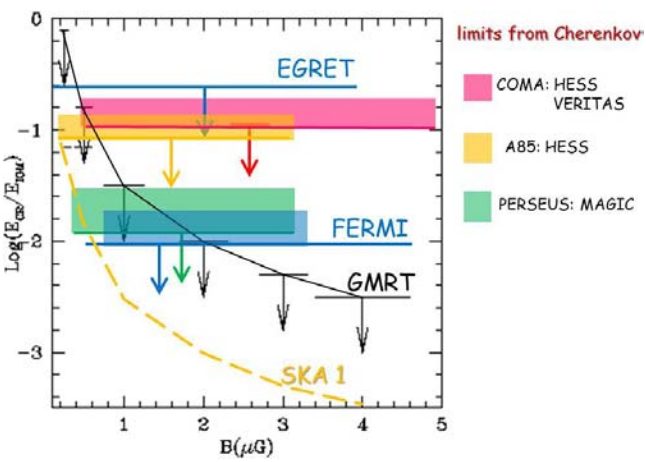

Fig. 10. A collection of representative upper limits to the ratio of the energy in CRp and thermal ICM as derived from γ-ray and radio observations. Radio-based upper limits depend on the magnetic field strength in a Mpc^3 volume. Limits from observations with Cherenkov telescopes include the case of Coma,[197,199] A85[29] and Perseus.[31] In Refs. 29 and 197 $\delta = 2.1$ and a spatially constant ratio of CRp and ICM energy densities are assumed. In the case of Coma[199] we report the limits obtained by these authors by adopting a spatial distribution and spectrum of CRp from numerical simulations. In the case of Perseus[31] the reported region (green) encompasses limits obtained using $\delta = 2.1$ and a spatially constant ratio of CRp and ICM energy densities and limits obtained by adopting a spatial distribution and spectrum of CRp from numerical simulations. Limits from EGRET and Fermi-LAT are taken from Ref. 26 and Refs. 32 and 33 respectively. In Refs. 26 and 33, limits are obtained assuming a spatially constant ratio of CRp and ICM energy densities, whereas we report the limits obtained by Ref. 32 by assuming the spatial distribution of CRp from simulations. Upper limits derived from radio observations are taken from Ref. 35. The sensitivity level to CRp from future SKA 1 observations is also reported for clusters at $z = 0.25$.

note however that current limits on the hard X-ray and γ-ray emission[30] from galaxy clusters exclude the possibility that the magnetic fields in the ICM are smaller than 0.1–0.2 μG. Weaker fields than these in clusters hosting giant radio halos would, as we explain in Sec. 5, necessarily require inverse Compton hard X-rays above current upper limits from the same CRe population responsible for the radio synchrotron emission.

4. Diffuse Synchrotron Radio Sources in Galaxy Clusters: Radio Halos and Relics

Steep spectrum ($\alpha \geq 1$, with $F(\nu) \propto \nu^{-\alpha}$), diffuse radio emission extended on cluster scales is observed in a number of galaxy clusters. The emission is clearly associated with the ICM and not individual sources, implying the existence of relativistic electrons and magnetic fields mixed with the ICM. Without entering in the details of the morphological zoology that is observed, see Refs. 37 and 38, in this section we focus on the two main classes of diffuse radio sources in galaxy clusters: radio halos and giant radio relies.

Halos and relics have different properties and presumably also a different origin. Radio halos are classified in *giant* (Fig. 11) and *mini radio halos* (Fig. 15), peaking

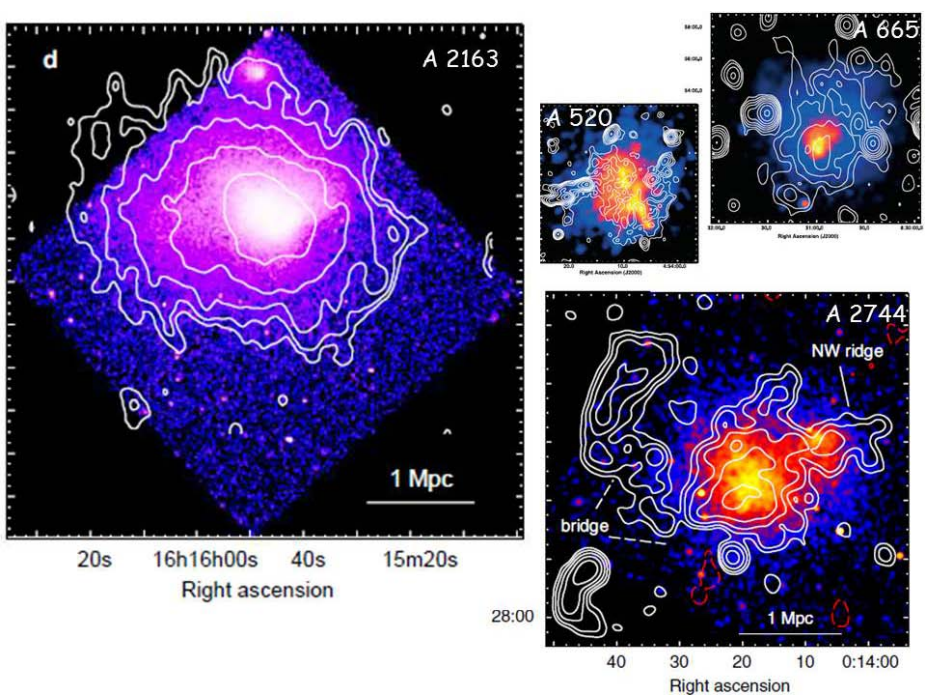

Fig. 11. Radio images of giant radio halos (contours) overlaid on the thermal X-ray emission of the hosting clusters. Images are reported with the same physical scale (credits: Giacintucci in prep. for A2163,[210] for A520 and A665,[211] for A2744).

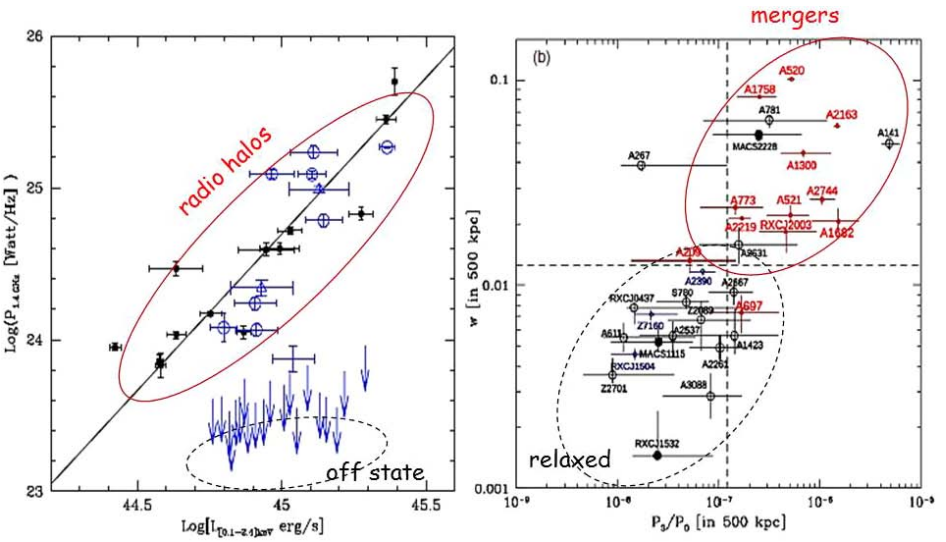

Fig. 12. (Color online) Left panel: distribution of galaxy clusters of the GMRT sample"[244] in the radio power — X-ray luminosity diagram, showing that clusters branch into two: giant radio halos (the merging systems in the left panel of the figure) and off state", undetected, systems (the relaxed systems in the left panel of the figure) (adapted from Ref. 248). Right panel: distribution of galaxy clusters in the centroid-shift variance w versus power ratio P_3/P_0 diagram. Mergers are expected in the top-right panel, relaxed systems in the bottom-left panel. Clusters hosting giant radio halos are reported in red (adapted from Ref. 68).

important step has been achieved in the last few years, thanks to meter wavelength radio observational campaigns at the GMRT[q] combined with observations at higher radio frequencies and in the X-ray band.[68,243–247] The high sensitivity surveys with the GMRT found that clusters with similar thermal X-ray luminosity, and presumably similar mass, branch into two populations, one hosting radio halos and a second one with no evidence for halo-type cluster-scale radio emission at the sensitivity level of current observations[35,248] (Fig. 12, left). Related to this finding, another observational milestone that has been achieved in the last decade is the connection between giant radio halos and the dynamics of the hosting clusters, with halos always found only in merging systems.[38,249] Firm statistical evidence of that has been recently obtained from combined radio — X-ray studies of galaxy clusters in the GMRT surveys[68,246] (Fig. 12, right). These studies have shown that the generation of giant radio halos occurs during mergers between galaxy clusters. This leads to a number of possible physical interpretations. The most obvious are that turbulence generated during cluster mergers may rapidly accelerate CRs (Sec. 2.2.2)[35,236,248] or that the cluster magnetic field can be amplified by the turbulence during these mergers.[239,250] Less obvious hypotheses to connect halos and mergers have been proposed, including the possibility that spatial diffusion

[q]http://gmrt.ncra.tifr.res.in/.

halos with very steep spectra that are undetected by radio surveys at higher frequencies and that should be discovered by observations at lower frequencies.[15,271,272,274] Such a hypothesis is based on turbulent acceleration models that predict that less energetic merger events (less turbulent) generate radio halos with very steep spectra. Since these less energetic mergers are more common, one can speculate that steep spectrum halos constitute a large population of halos that is presently invisible. According to present calculations that use the crude assumption that a *fixed* fraction of the cluster-merger energy goes into MHD turbulence available for particle acceleration on Mpc-scale, the LOFAR surveys should detect about 500 new radio halos. About half of these halos should have very steep spectra.[272,274] Despite their still-early development and need for greater sophistication, current models have been able to make some notable predictions.[u] For instance, reacceleration models predict that the shape of the Luminosity Functions of radio halos change with

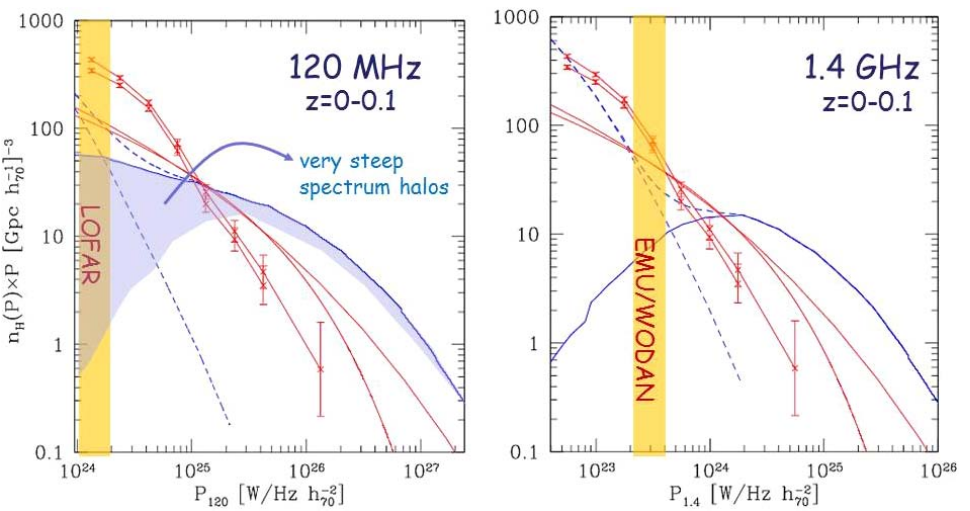

Fig. 14. (Color online) Radio luminosity functions of giant radio halos at $z = 0$–0.1 predicted by different models at 1.4 GHz (right) and 120 MHz (left). Blue lines are based on turbulent reacceleration models (solid line) and secondary emission (thin dashed lines) from "off state" systems (i.e. undetected halos in Fig. 12), the thick dashed-lines represent the sum of the two contributions (adapted from Ref. 272). Red-solid lines are from Ref. 275 while the red-points are from numerical simulations by Ref. 273 that are based on secondary models and assume that 10% of systems host radio halos (note that those simulations include both giant and mini halos). The blue region in the left panel shows the contribution to the luminosity function at 120 MHz due to very steep spectrum halos that are predicted in the turbulent reacceleration model and do not contribute at higher frequency. The nominal sensitivity level of LOFAR and EMU/WODAN surveys is also reported.

[u]We note that, independent of the theoretical scenario that is adopted for the origin of radio halos, predictions of the formation rate of radio halos and their number counts are severely limited by uncertainties in the properties of cluster magnetic fields — including their evolution with cluster mass and cosmic epoch — and CR dynamics.

observing frequency due to the contributions of the expected population of steeper-spectrum halos at lower frequencies (Fig. 14). This differs from predictions based on other scenarios, including the hadronic model, where all halos should have as a first approximation similar spectra (independent of the mass of the hosting clusters and of the energy released during mergers), and provides a valuable way to put constraints on the origin of these sources with future radio surveys. In particular, as shown in Fig. 14, the most powerful way will be probably the combination of LOFAR surveys, at low frequencies, with future surveys with ASKAP or Apertif,[v] at higher frequencies.

4.3. *Mini halos*

In addition to the disturbed, merging clusters that have been found to host giant radio halos, a number of relaxed, cool-core clusters host faint, diffuse radio emission with a steep spectrum and a size comparable to that of the cool-core region[38] (Fig. 15), so substantially smaller than the giant halos. As a first approximation one might have thought these sources as a version of giant radio halos scaled on smaller scales of the order of few 100 kpc in size rather than Mpc size. However, the two

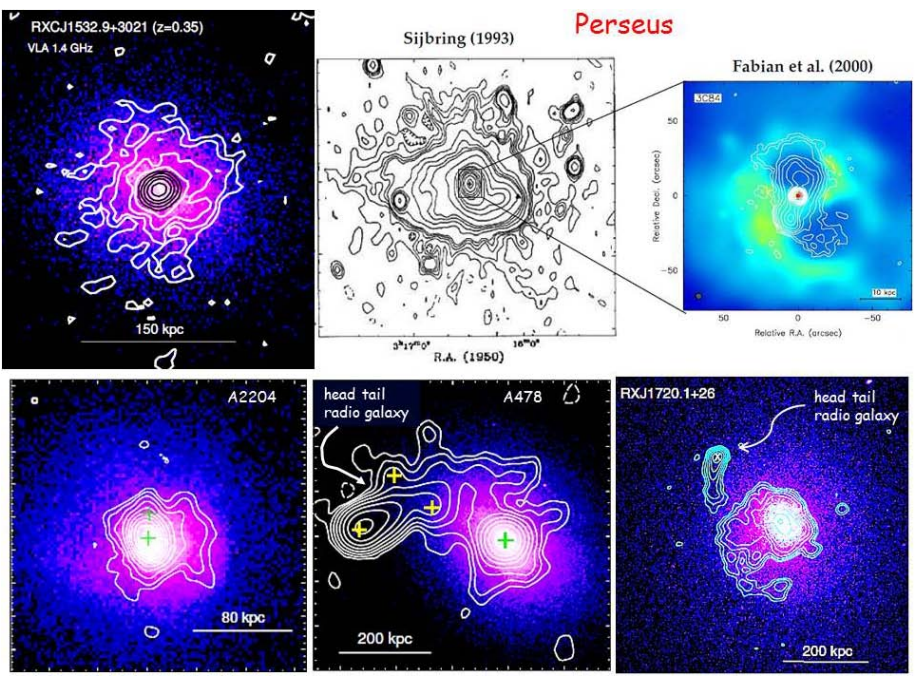

Fig. 15. Images of radio mini halos (contours) and the X-ray emission from the hosting clusters (colors). Credits[212]: for RXCJ1532, A2204, A478, Giacintucci in prep. for RXCJ1720, and in Ref. 213 for Perseus.

[v]http://www.astron.nl/general/apertif/apertif.

A similar evolution could be driven by the evolution (amplification and dissipation) of the magnetic field in the cluster core and periphery in response to mergers.[239,250]

Observations with the next generation of observational facilities and similar advances in numerical simulations will hopefully clarify these issues in the near future.

4.4. *Giant radio relics*

Some merging clusters host peripheral giant radio relics. As in the case of giant radio halos, a few tens of giant relics have been discovered so far. Radio relics differ from radio halos in the morphologies, peripheral locations and polarization (typically being up to 30% level in integrated linear polarization)[38] (Fig. 16). These properties provide a clear starting point in establishing their origin. Specifically, there is broad consensus that the giant radio relics trace shocks outside cluster cores, probably relatively strong merger shocks, where the emitting CRe can be accelerated or reaccelerated.[23,39,97–99,196,214,293–299] This model is based on the physics described in Sec. 2.2.1.

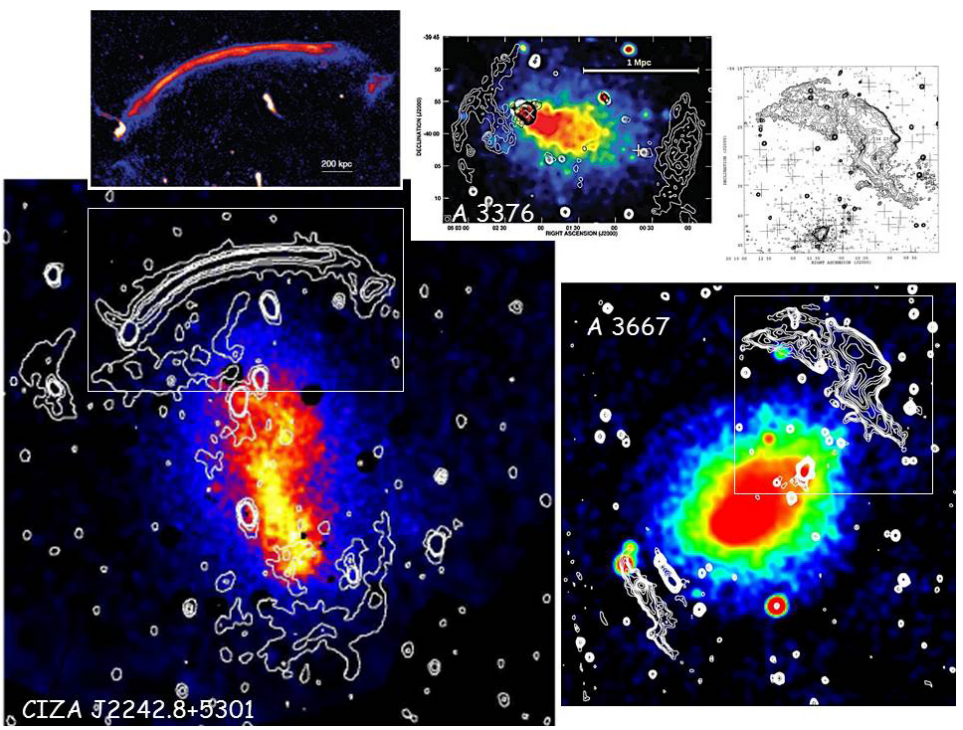

Fig. 16. Images of giant radio relics (contours) overlaid on the X-ray emission from the hosting systems (colors). The three radio relics are reported with the same physical scale. Upper-left and upper-right panels highlight the high-resolution radio images of the northern relics in CIZA2242 and A3667, respectively (credits: Refs. 214 and 215 for CIZA2242, Ref. 216 for A3667 and Ref. 217 for A3376).

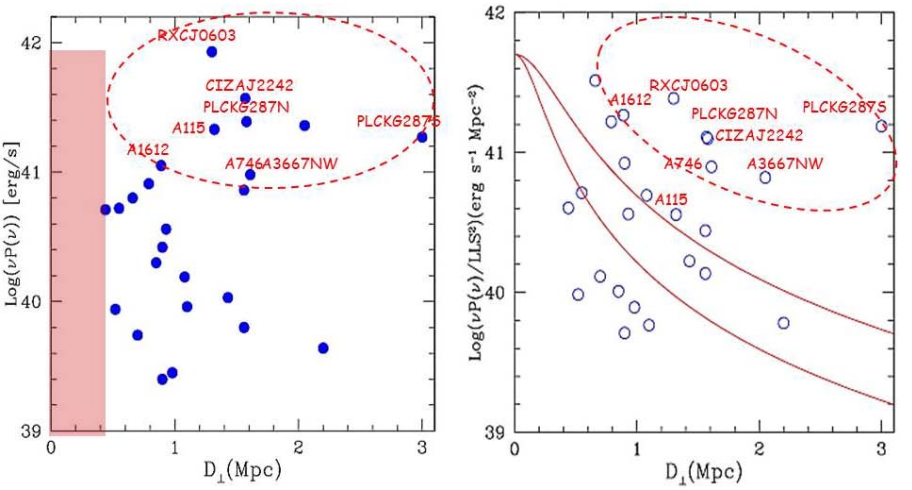

Fig. 18. Left panel: the synchrotron radio luminosity ($\nu P(\nu)$ evaluated at 1400 MHz) as a function of projected distance from cluster center for 25 giant radio relics with unambiguous classification. Data are taken from the compilations in Refs. 38 and 42, although we only use the 25 sources that can be "unambiguously" classified as giant radio relics. Right panel: the synchrotron radio luminosity ($\nu P(\nu)$ evaluated at 1400 MHz) per unit relic-surface area as a function of projected distance for the same relics in the left panel. Solid lines mark reference radial behaviours of the kinetic energy flux per unit area through shocks with equal velocity (in arbitrary units); they are obtained using typical beta-models for the gas-density distribution in the hosting clusters. The pink vertical band in the left panel marks the typical minimum distance where giant radio relics are found.[313]

Another problem faced by the standard scenario where relics originate from shock acceleration of thermal particles is that in several cases the observed radio spectrum is flatter than that expected from DSA by assuming the Mach number of shocks derived from X-ray observations (Eq. (3)).[306,308] For example, the well studied relic in CIZA J2242.8+55301 has a radio spectra at the putative shock location $\alpha_{\rm inj} = (\delta_{\rm inj} - 1)/2 = 0.6$ (so, $\delta_{\rm inj} = 2.2$), implying from Eq. (3) a rather large shock Mach number $M = 4.6$,[214] if the radiating electrons represent a locally injected population. On the other hand, X-ray observations with Suzaku derived a Mach number $\sim$3 from the temperature jump at the relic,[306] which would imply $\alpha_{\rm inj} \simeq 0.75$. In this respect it is worth mentioning that numerical simulations show variations of the Mach number over shocks[314] that potentially might produce some differences in the shock Mach numbers derived from X-rays (temperature or density jumps) and from radio. In this case the radio Mach number would be biased high because synchrotron emission is likely to be locally stronger in regions with higher Mach number.

In principle, all the challenges discussed above can be naturally circumvented by adopting a scenario where radio relics are generated by the reacceleration of pre-existing (seed) CRe at merger shocks.[97,298,299] If a pre-existing population of CRs with a hard (flat) spectrum passes through such weak shocks, DSA can enhance the energy content of those CRs by a factor of a few. This makes DSA reacceleration